



OPEN

## Multiphysics study on the higher harmonic RF cavity for the Iranian Light Source Facility's storage ring

A. Sadeghipanah<sup>1,2</sup>, S. Ahmadiannamin<sup>1,2</sup>, M. Ostovar<sup>1,3</sup>✉, S. Talebi Motlagh<sup>1,2</sup>, A. Babaie<sup>4</sup>, V. Moradi<sup>1</sup>, J. Roohi<sup>1</sup> & B. A. Arand<sup>3</sup>

Higher harmonic cavities are widely used in low-emittance and high-current synchrotron storage rings to increase the stored beam's lifetime and eliminate the coupled bunch instabilities. These parameters have an essential effect on the quality of synchrotron radiation and the machine's stability. Higher harmonic cavities of the Iranian light source facility are passive, capacitive-loaded structures designed to operate at 300 MHz. These cavities can operate in the beam current range of 50–400 mA. This article comprehensively discusses analytical calculations and simulations of beam dynamics, electromagnetic, thermomechanical, and vacuum aspects of the Iranian Light Source Facility's higher harmonic cavities. The engineering drawings are finalized after many technical discussions according to the presented results, and the fabrication process of the higher harmonic cavity has been started accordingly. The low-power RF measurement results of the first developed prototype are reported in the final section.

**Keywords** Synchrotron radiation, Higher harmonic cavity, Tuning mechanisms, Electromagnetic simulations, Thermo-mechanical simulations, Vacuum simulations

The Iranian Light Source Facility (ILSF) is a 3 GeV low-emittance synchrotron light source laboratory dedicated to scientific research, featuring a very bright X-ray source for a wide range of applications. This project is one of the most significant scientific infrastructures in Iran and has the potential to become a regional scientific hub in the near future. It is currently in the final phase of detailed design with NEG-coated vacuum chambers<sup>1,2</sup>.

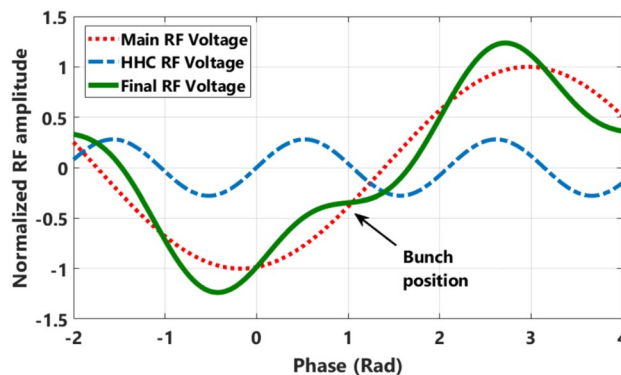
The injector for this light source consists of a 2.5 MeV thermionic RF gun, an alpha compressor magnet, and three Linac tubes, which accelerate the beam to a maximum energy of 150 MeV before it enters the booster synchrotron<sup>3,4</sup>. After acceleration in the booster synchrotron to an energy of 3 GeV, electron bunches with a length of 7.9 mm are entered and stored in a 528 m long storage ring with a five-bend achromatic magnetic lattice to a maximum beam current of 100 mA for the first phase of operation<sup>5,6</sup>. The storage ring is designed to implement 30 different beamlines for various research purposes at the final phase of operation. The parameters of the ILSF storage ring are listed in Table 1.

Touschek scattering instability is a key limiting factor in achieving high charge density for electron bunches in storage rings. An increase in the charge density of electron bunches results in a higher collision probability among electrons within the bunch. These collisions transfer transverse momentum to longitudinal momentum, leading to the loss of these particles and a decrease in their lifetime<sup>7</sup>. Many third and fourth-generation synchrotron light sources employ dual RF systems to address these detrimental phenomena. In these systems, two types of RF cavities operate at different frequencies within the storage ring: one at the fundamental frequency of the RF system and the other at the third, fourth, or fifth harmonic of that frequency. The second type of cavity, which operates at the higher harmonic of the fundamental RF frequency, is known as the Higher Harmonic Cavity (HHC). By adding HHCs to the storage ring's RF system, the voltage slope around the synchronous phase flattens (see Fig. 1), and the length of the electron bunches increases without any significant deterioration of the bunch's energy spectrum. This increase in bunch length is desirable for several reasons: it reduces charge density in the electron bunch and extends the Touschek lifetime by three to four times. Additionally, the frequency spread of synchrotron oscillations broadens, triggering Landau damping and significantly decreasing coupled bunch instabilities<sup>7–9</sup>.

HHCs can operate in both passive and active modes. In passive mode, since there is no need for an external generator, HHCs are easier to manufacture, simpler to operate, and more cost-effective. However, the active

<sup>1</sup>Iranian Light Source Facility (ILSF), Institute for Research in Fundamental Sciences (IPM), Tehran, Iran. <sup>2</sup>School of Particles and Accelerators, Institute for Research in Fundamental Sciences (IPM), Tehran, Iran. <sup>3</sup>Department of Electrical and Computer Engineering, Tarbiat Modares University (TMU), Tehran, Iran. <sup>4</sup>Radian Applications Department, Shahid Beheshti University (SBU), Tehran, Iran. ✉email: mohammad.ostovar@ipm.ir

Parameter	Value	Unit
Beam energy	3	GeV
Beam current (first phase of operation)	100	mA
Emittance	0.28	nm-rad
Circumference	528	m
RF frequency	100	MHz
Maximum RF voltage	1.5	MV
Number of dipole magnets	100	–
Number of quadrupole magnets	240	–
Number of sextupole magnets	320	–
Bunch length (without higher harmonic cavities)	7.9	mm

**Table 1.** Main parameters of the ILSF storage ring.**Fig. 1.** (Color) Main RF voltage (red dotted line), HHC RF voltage (blue dot-dashed line), and final RF voltage (green line).

Synchrotron name	Cavity type	Operating mode	Harmonic frequency	Storage ring current	Bunch lengthening factor
MAX IV	Normal-conductor	Passive	3 × 100 MHz	500 mA	× 5
ALBA II	Normal-conductor	Active	3 × 500 MHz	300 mA	× 2.55
ELETTRA II	Super-conductor	Passive	3 × 500 MHz	400 mA	× 2.5–3
HEPS	Super-conductor	Active	3 × 166.6 MHz	200 mA	~ × 6

**Table 2.** HHC specifications for certain advanced synchrotrons.

mode offers better controllability and enables greater bunch lengthening. The material of HHCs can be either a normal-conductor or a super-conductor. Super-conductors offer higher shunt impedance compared to normal-conductors; as a result, they can be more effective in enhancing bunch lengthening<sup>8</sup>. Nevertheless, the same overall lengthening effect can be achieved with normal-conductor HHCs by using a larger number of cavities. HHC specifications for certain advanced synchrotrons are presented in Table 2<sup>10–14</sup>.

There are certain restrictions when selecting the frequency of HHCs, particularly regarding the dimensions of the vacuum chambers, which can reduce the shunt impedance of the HHC. Several factors, including the specific requirements of the accelerator, beam dynamics, and the desired performance, can influence the choice of harmonic number for an HHC. Due to the lower mechanical and tuning complexity of the third harmonic of the fundamental frequency, along with its capability to provide the desired bunch lengthening, it is typically used in synchrotron storage rings<sup>8</sup>. However, the fourth harmonic has also been utilized and studied in some synchrotrons<sup>15,16</sup>.

This paper presents inclusive considerations of all aspects of the analytical, electromagnetic, thermo-mechanical, and vacuum calculations for ILSF's HHCs. The following sections outline the calculation of HHC parameters and electromagnetic design, as well as beam dynamics analysis related to cavity performance, simulation, and determination of higher-order modes, thermo-mechanical simulations, and vacuum system calculations. Finally, the fabrication and low-power RF measurements of the first prototype HHC are described.

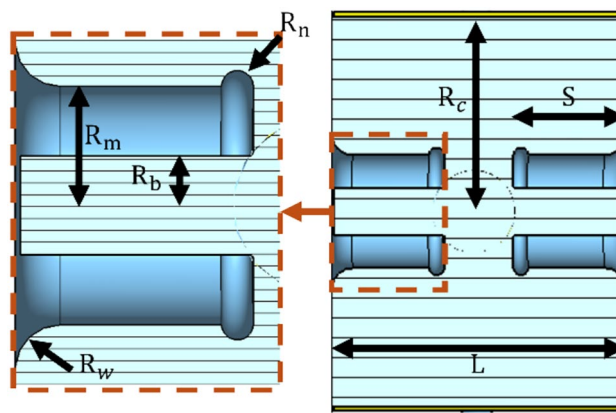


**Fig. 2.** A 3D model of the HHC structure.

Parameter	Value (mm)
$R_c$	207.5
$S$	115
$L$	307.5
$R_n$	8
$R_m$	28
$R_b$	25
$R_w$	22.5

**Table 3.** Dimensions of the HHC structure.

### Electromagnetic simulations and design

The ILSF's HHCs are designed to operate in passive mode because it is easier to fabricate and operate and less costly<sup>8</sup>. Similar to the light sources examined in “Introduction”, the third harmonic of the fundamental frequency (300 MHz) has been selected as the operating frequency for our HHC. This mode provides sufficient bunch lengthening, but its frequency is not high enough to propagate through the vacuum chambers. A capacitive-loaded structure, with two mushroom-shaped structures on each end wall, has been selected for the ILSF's HHC to minimize cavity dimensions and reduce fabrication costs (see Fig. 3). Furthermore, the gap between the fundamental frequency and HOMs in capacitive-loaded cavities is relatively large, which improves reliability and simplifies the design of HOM dampers<sup>17</sup>. Although passive super-conductor and active normal-conductor HHCs have greater capability than passive normal-conductor HHCs for bunch lengthening, our beam dynamics simulations show that normal-conductor HHCs provide effective bunch lengthening for ILSF's storage ring (see “Beam dynamics calculations”). Other instabilities can be suppressed using the longitudinal feedback system. Therefore, to minimize complexity and manufacturing costs, passive normal-conductor HHCs are selected for the ILSF.

The ILSF's HHCs operate in the TM010 resonance mode. The design of the HHC aims to maximize the quality factor and shunt impedance at the target resonance frequency of 300 MHz. There is an optimal level of shunt impedance that results in maximum bunch lengthening conditions. By increasing the shunt impedance during the electromagnetic design process, this optimal level can be achieved with fewer cavities in the storage ring (see “Bunch lengthening” for more details). Additionally, as the cavity's quality factor increases, less power is dissipated on the cavity's inner surfaces for a given voltage, which reduces the water flow rate required in the cooling pipes, making the cooling system more straightforward and more cost-effective. “Thermo-mechanical simulations and design” provides further details about the HHC's thermal analysis.

Initial 2D calculations of the HHC are conducted using Poisson Superfish software (version 7.1)<sup>18</sup> to estimate the preliminary dimensions of the structure and their frequency tolerances. Since Poisson Superfish<sup>18</sup> is limited to symmetrical structures, CST Studio Suite software (version 2024)<sup>19</sup> is employed to evaluate a more realistic structure model with all its ports (see Figs. 5 and 16). The maximum surface E-field of the cavity is approximately 8.5 MV/m, which is significantly lower than the Kilpatrick criterion for the maximum potential breakdown at the frequency of 300 MHz (17.5 MV/m)<sup>20</sup>. The power dissipated on each surface of the structure is also calculated, and this data is later used for thermal and mechanical analysis. A 3D model of the HHC structure and its dimensions are shown in Fig. 2 and Table 3, respectively. Furthermore, the electric and magnetic field profiles calculated in CST Studio Suite<sup>19</sup> are shown in Fig. 3.

The simulation results for resonant frequency, quality factor, and shunt impedance using Poisson Superfish<sup>18</sup> and CST Studio Suite<sup>19</sup> are presented in Table 4. The differences between the results from these two software

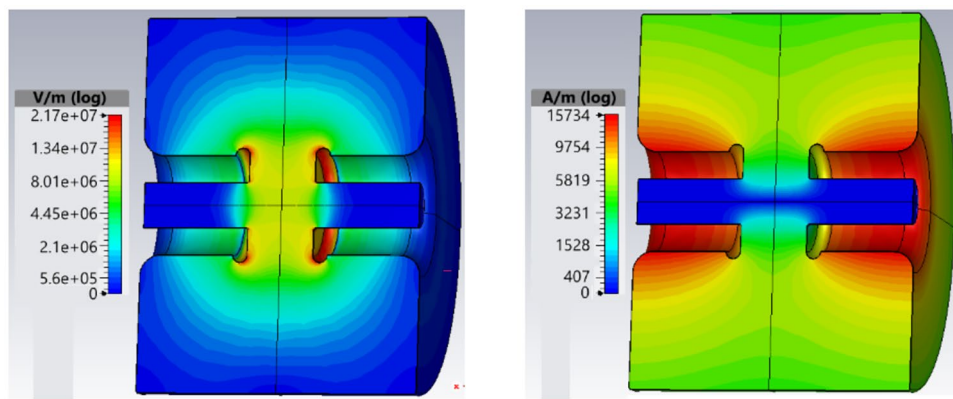


**Fig. 3.** (Color) CST studio suite simulation results: (left) Electric field and (right) magnetic field profiles.

Parameter	Superfish	CST studio suite (with ports)	CST studio suite (without ports)
Frequency (MHz)	301.23	300.15	299.77
Shunt impedance ( $M\Omega$ )	6.93	6.92	6.95
Quality factor	23,210	23,000	23,100

**Table 4.** RF parameters of the HHC.

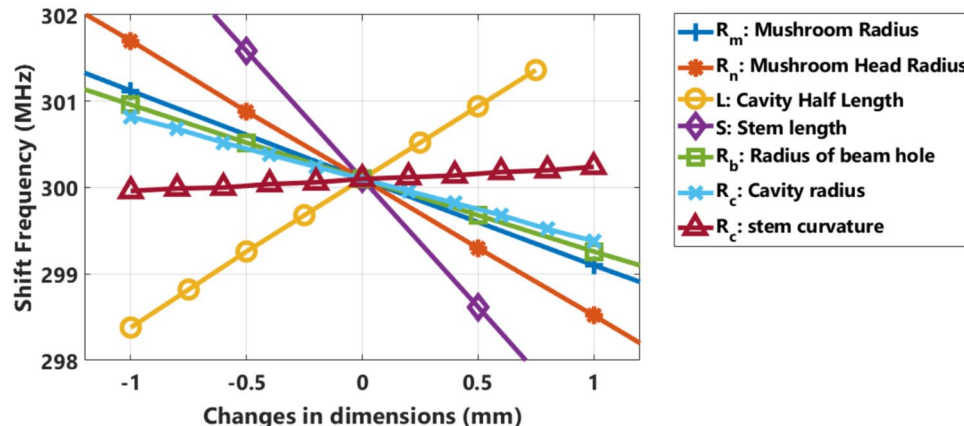


**Fig. 4.** (Color) Sensitivity analysis of the HHC's dimensions.

are likely due to the presence of ports in the CST Studio Suite<sup>19</sup> simulations (see Figs. 5 and 22). Since the HHC operates in passive mode, its voltage and power loss are determined by the beam current (see Eqs. 1 and 4).

The maximum electric field is located at the edges of the mushroom head, making these areas the surfaces that are most susceptible to the RF breakdown, as illustrated in Fig. 3. Properly finishing these surfaces with the least amount of filler spread on these areas during brazing is crucial for improving RF conditioning and minimizing most breakdown trips. Additionally, the strongest magnetic field, which primarily causes thermal loss on the inner surfaces of the cavity, is found on the stem of the mushroom and its connection to the end wall. Consequently, the design of the cooling system in this area is particularly important.

Another critical study in the design of the HHC involves evaluating how the tolerances of geometric parameters impact the resonance frequency. These studies aid in developing the optimal fabrication process while fine-tuning the cavity's dimensions and selecting the most effective method of initial surface machining to achieve the desired frequency before permanently assembling all components. The impacts of the geometric parameters on the resonance frequency are shown in Fig. 4. According to the simulations, the most significant frequency shift is linked to the length of the mushroom stem (S). In contrast, the least sensitivity is related to the curvature of the stem's connection to the end wall ( $R_w$ ).

The HHC features five distinct ports: one for a plunger (or RF power coupler during conditioning), two for the electron beam's input and output, two for vacuum pumps, two for HOM-suppressing antennas, and two for field sampling antennas (see Fig. 22). The field sampling antennas are integrated into the HHC's body to

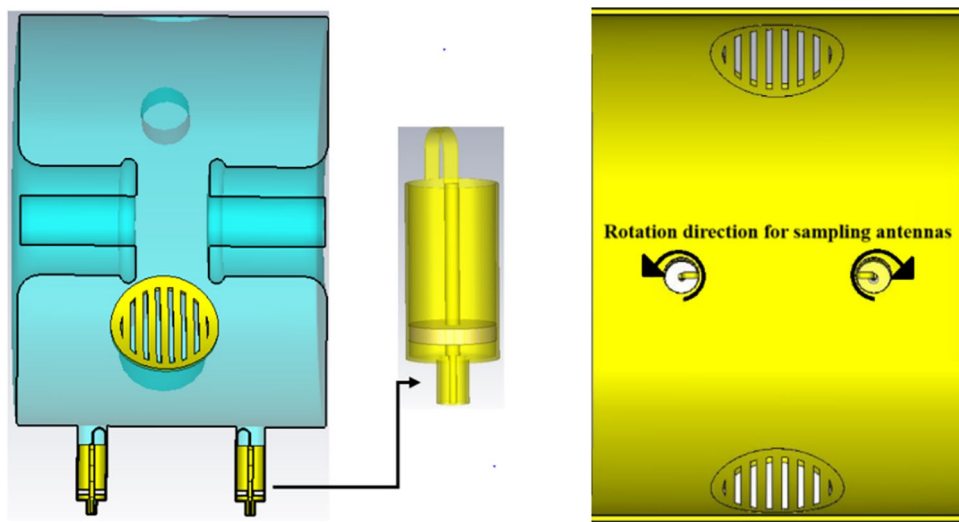


**Fig. 5.** Simulation model: (left) side view and (right) inside view of the sampling antennas.

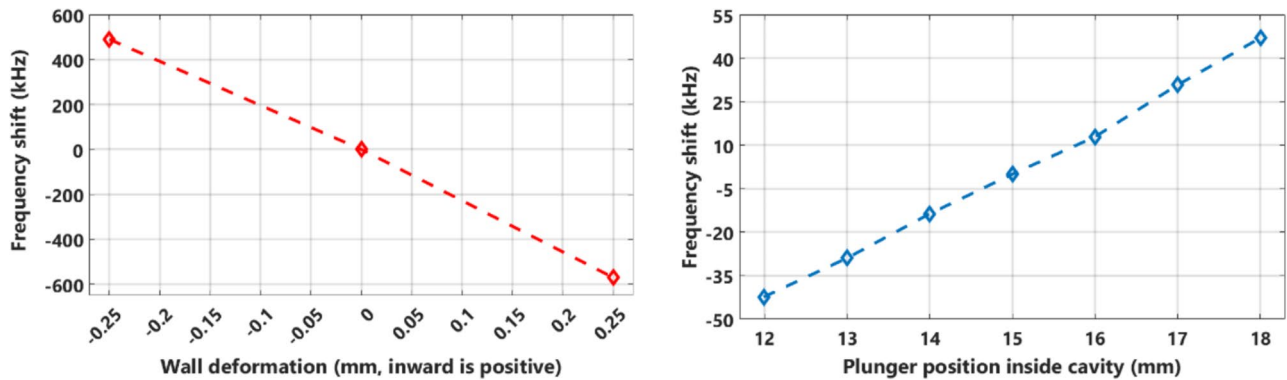


**Fig. 6.** Frequency tuning range: (left) end wall displacement and (right) plunger penetration.

measure and control the voltage and frequency of the cavity, as well as to assess the parameters of the electron bunches. Figure 5 presents the CST Studio Suite<sup>19</sup> simulation model used to optimize the dimensions of these sampling antennas. Following our previous investigations into ILSF's 100 MHz RF cavity<sup>17,21</sup>, we consider two frequency tuning mechanisms based on plunger penetration and side wall displacement for the HHC. The side wall displacement, resulting from substantial variations in the cavity's capacitance, affects the frequency more significantly than the plunger mechanism. The simulation results for the frequency shift of the HHC using both end wall and plunger displacement methods are depicted in Fig. 6.

Each 0.1 mm displacement of the end wall generates a frequency change of about 112 kHz, while each millimeter displacement of the plunger results in a frequency variation of about 12.5 kHz. The initial position of the plunger is 15 mm from the inner surface of the cavity. Pushing the end wall inward decreases the cavity frequency, while pulling it outward increases it. Additionally, the frequency increases as the plunger moves toward the center of the cavity and decreases with outward displacement. The diameter of the plunger is 88 mm. The plunger in the structure serves two distinct purposes. The first is to shift the frequency of HOMs to mitigate their destructive effects<sup>18</sup>. It can also detune the HHC completely and eliminate its impact on the RF system.

A simple RF power coupler is designed for HHC's RF conditioning. A 3-1/8 inch coaxial waveguide is chosen for the transmission line, and the transition area between the ceramic window and the coaxial waveguide to the coupler loop is optimized to achieve critical coupling. The permittivity of the ceramic window is  $\epsilon_r = 9.4$ , and its thickness is 5 mm. The coupling loop is also set at a 45-degree angle to the HHC's horizontal axis to obtain the critical coupling condition. The simulated geometry of the power coupler and the reflection scattering parameter are shown in Fig. 7.

## Beam dynamics calculations

### Bunch lengthening

Since the ILSF's HHC is designed to operate in passive mode, it relies solely on the electron beam to generate the RF voltage. Figure 8 illustrates the impact of HHC's frequency tuning on the impedance and phase of its

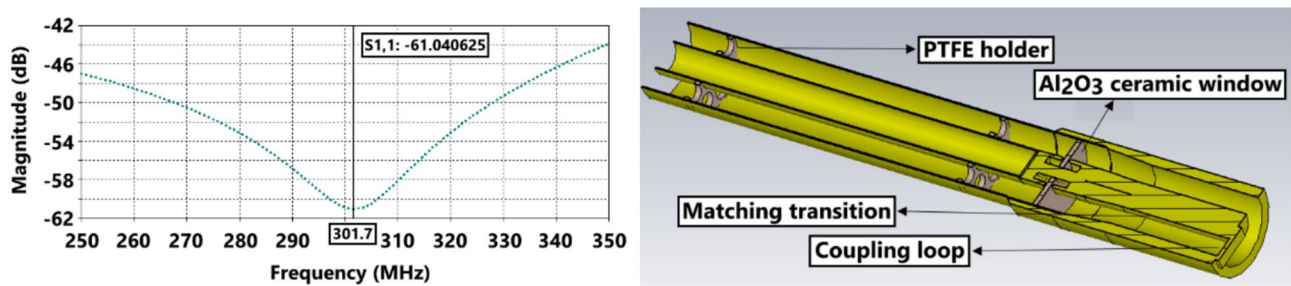


**Fig. 7.** RF power coupler: simulated geometry (right) and the reflection S-parameter (left).

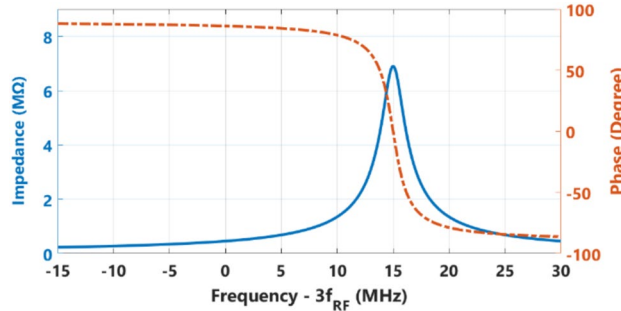


**Fig. 8.** (Color) Impact of HHC's frequency tuning on generated RF voltage: Impedance (solid line-blue) and phase (dashed line-red) of HHC for various frequency shifts from the third RF harmonic.

fundamental mode. As depicted, the amplitude and phase of the HHC's voltage are adjusted by tuning its fundamental mode. To increase the bunch length, the HHC should be tuned above the 3rd harmonic of the RF frequency so that the phase difference between the electron beam and the HHC's voltage is approximately 90 degrees. The HHC's voltage generated by the beam is given by<sup>22</sup>

$$V_H = 2I_{beam}FR_s \cos\varphi_H \cos(3\omega_{RF}t - \varphi_H), \quad (1)$$

where  $R_s$  is the HHC's shunt impedance,  $\varphi_H$  is the phase difference between the electron beam and the HHC's voltage given by

$$\tan\varphi_H = 2Q \left( \frac{\omega_H - 3\omega_{RF}}{\omega_H} \right), \quad (2)$$

and  $F$  is the bunch form factor given by

$$F = e^{-(3\omega_{RF}\sigma_\tau)^2}. \quad (3)$$

The power loss within the cavity walls can also be achieved by

$$P_{loss} = \frac{V_H^2}{2R_s}, \quad (4)$$

and the maximum bunch lengthening conditions can be achieved at the optimal shunt impedance

$$R_{s,opt} \approx \frac{V_{rf} \tan\varphi_H}{6I_{dc}} \quad (5)$$

For the ILSF's storage ring, the RF voltage is 1.1 MV, and for a phase difference of approximately 97 degrees between the electron beam and the HHC's voltage at the beam current of 100 mA, the optimal shunt impedance is slightly less than 15 MΩ. This optimal level can be achieved utilizing three HHCs in the storage ring.

However, the shunt impedance and phase of the HHC cannot be adjusted independently, and maximum bunch lengthening can only occur at a specific beam current. In other words, the final bunch length depends on the beam current (see Fig. 9). This limitation is the main disadvantage of employing a passive HHC structure. For the ILSF's first phase of operation, i.e., a beam current of 100 mA, the optimal HHC phase based on Eq. (2) is 98 degrees, and the HHC voltage amplitude can be determined accordingly.

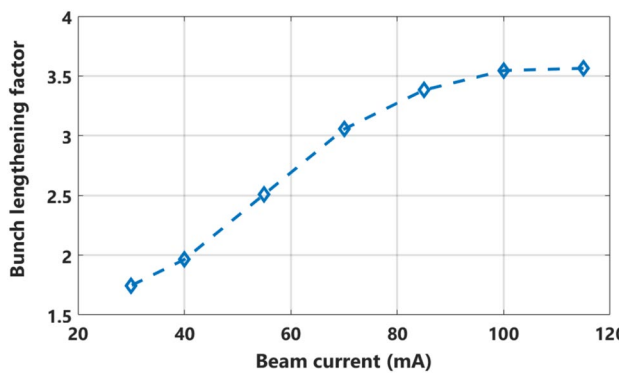


**Fig. 9.** Bunch lengthening factor changes with the beam current for the ILSF storage ring with HHCs, calculated using ELEGANT<sup>23</sup>.

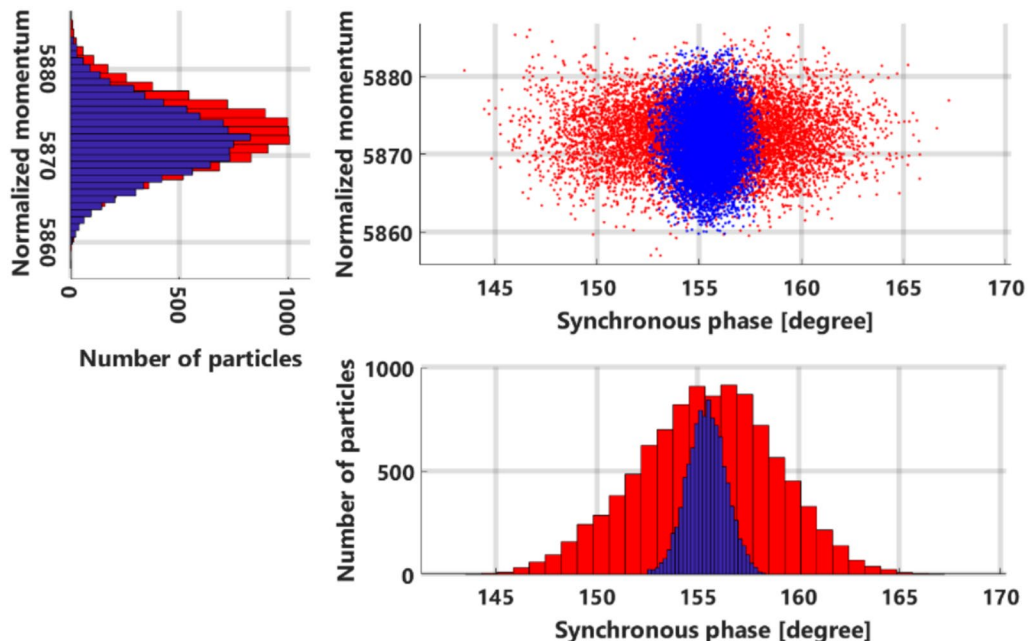


**Fig. 10.** (Color) Longitudinal particle distribution, along with phase and momentum histograms, for a single bunch, without (blue) and with (red) the HHCs present in the storage ring, at a 100% filling factor.

Particle tracking simulations using the ELEGANT code (version April 9, 2024)<sup>23</sup> are conducted to examine the effects of the ILSF's HHC on bunch length. The HHCs with specifications described in “[Electromagnetic simulations and design](#)” are inserted into the ILSF's storage ring. Simulations are carried out for three different filling pattern scenarios: all RF buckets in the storage ring are evenly filled with electron bunches, only 80% of the RF buckets are filled as a single bunch train, and 80% of the RF buckets are filled with four consecutive bunch trains spaced equally apart. Our initial design for the ILSF's filling pattern is the second scenario (80% of the RF buckets as a single bunch train). Since the third scenario (80% of the RF buckets as four consecutive bunch trains) can provide a more stable RF voltage inside the HHC, it is presented as an alternative for further study. If studies indicate that the third scenario offers better overall performance, it will replace the current choice as the preferred filling pattern.

Figure 10 shows the longitudinal particle distribution in a bunch before and after tuning the HHCs to the optimal frequency for the scenario in which 100% of the RF buckets in the storage ring are evenly filled. As observed, a three to four-fold increase in bunch length can be achieved by utilizing three HHCs in the storage ring, tuned to the phase of 96 degrees. Since all RF buckets are filled evenly, the beam current remains symmetric, resulting in all bunches in the storage ring having the same length.

In the scenario where 80% of the RF buckets are filled as a single bunch train, there is a 360 ns gap between consecutive bunch trains. The HHC's voltage dampens during this gap, causing a transient voltage rise at the start of each bunch train. The voltage takes approximately 300 ns to reach its final steady-state value, resulting in the first 30 bunches of each train experiencing suboptimal bunch lengthening. These results are presented in Fig.

11. After the 30th bunch, the HHC's voltage achieves its final amplitude, and the bunch length remains constant. The maximum bunch lengthening is again attained for a phase of 96–97 degrees.

In the final scenario, 80% of the RF buckets are filled again, but the train is divided into four consecutive bunch trains spaced equally apart. This time, the gap between consecutive bunch trains is only 90 ns, preventing the HHC's voltage from dampening thoroughly, which results in a semi-uniform longitudinal particle distribution throughout all bunches in the storage ring. The results for the first and last bunches of each train are shown in Fig. 12. The maximum bunch lengthening is again attained for a phase of 96–97°, and the final bunch length is slightly larger than in the previous scenario. Table 5 summarizes the bunch lengthening calculations for the three different filling scenarios.

According to Eq. (2), to attain a phase shift accuracy of about 1 degree, the frequency tuning precision must be 9 kHz or less for the HHC. Based on the simulation results shown in “[Electromagnetic simulations and design](#)”, this tuning accuracy can be achieved with a plunger displacement precision of 0.7 mm. Improving the

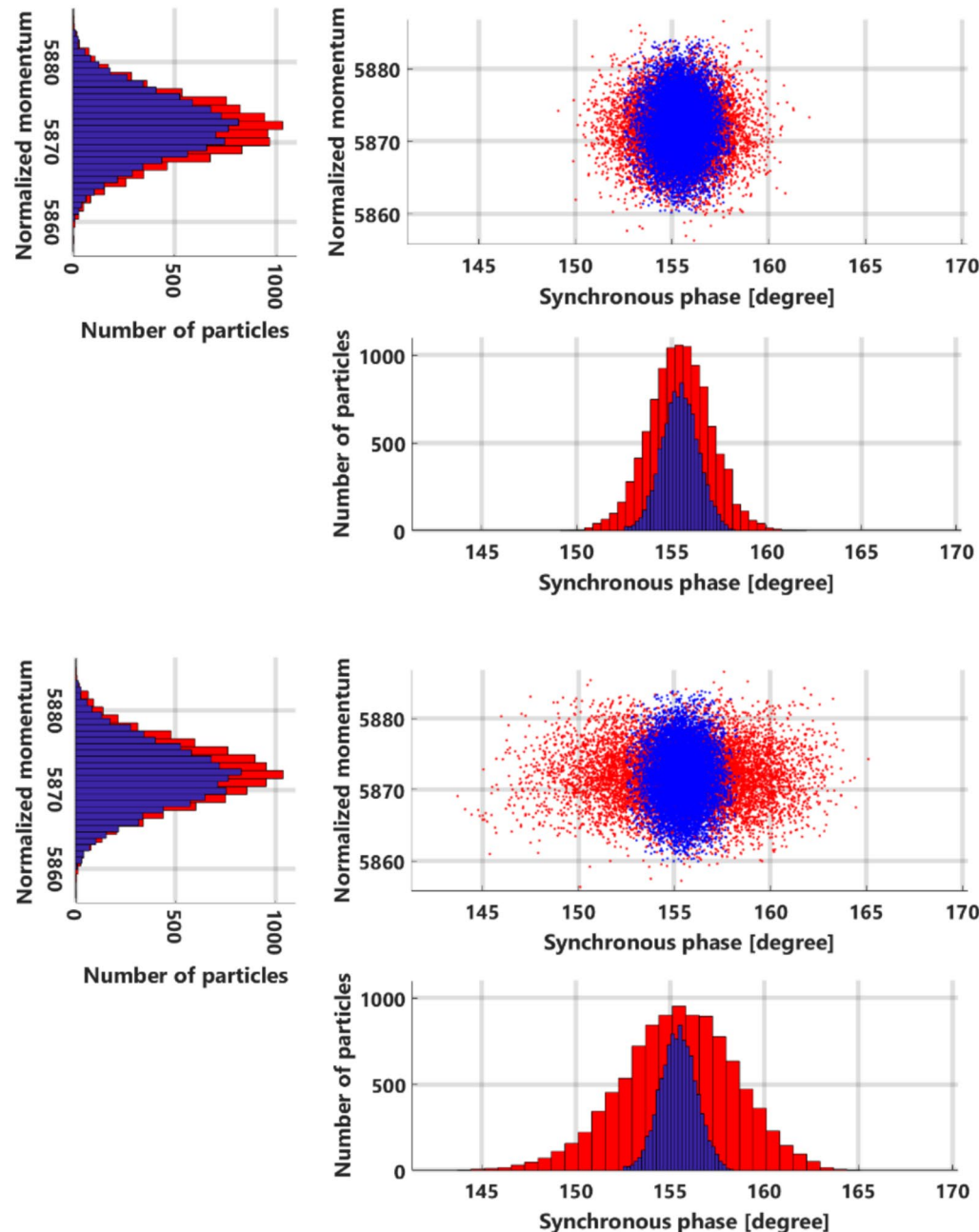


**Fig. 11.** (Color) Longitudinal particle distribution, along with phase and momentum histograms, for a single bunch, without (blue) and with (red) the HHCs present in the storage ring for an 80% filling factor as a single train, for the 1st (top) and 30th (bottom) bunches of the train.

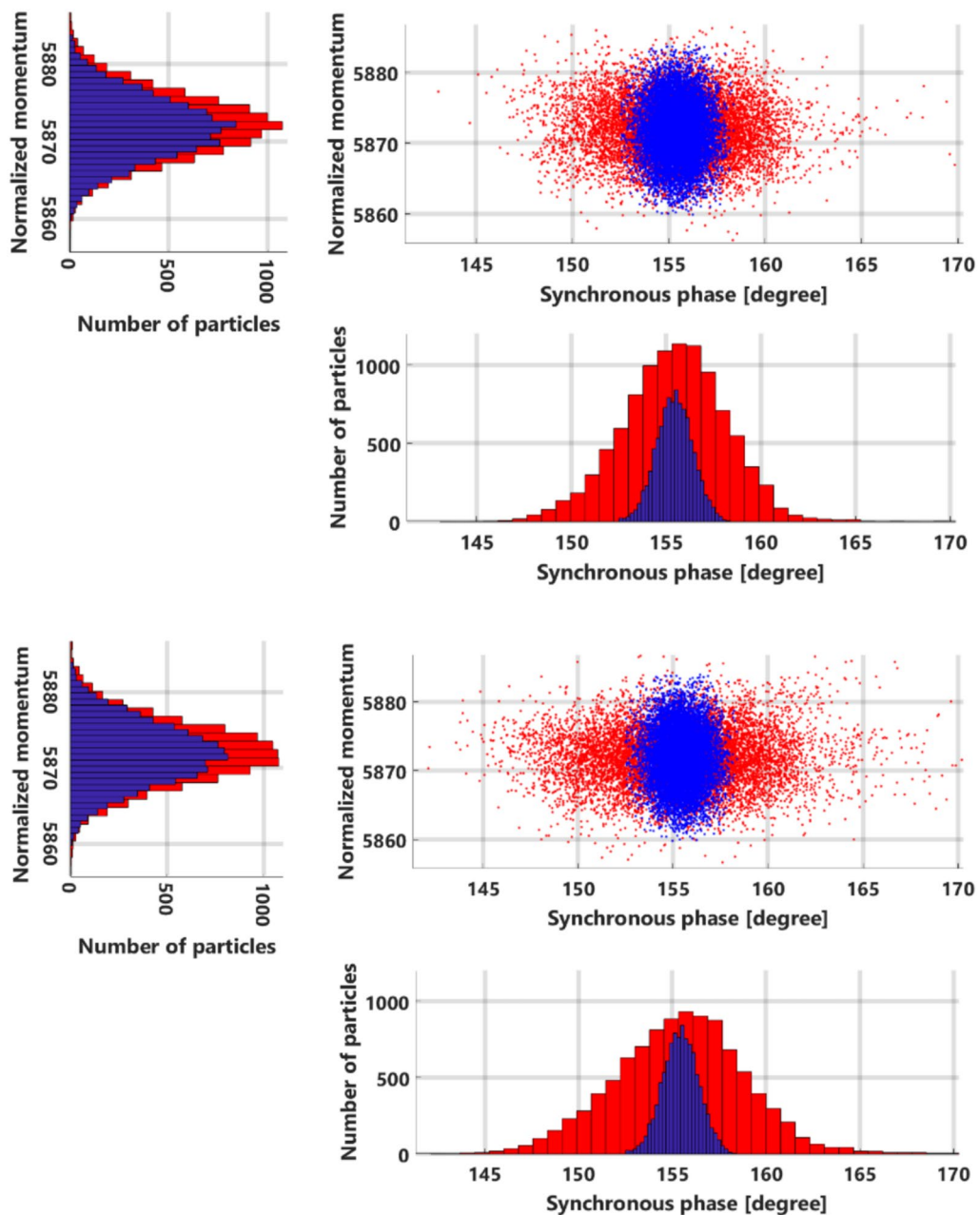


**Fig. 12.** (Color) Longitudinal particle distribution, along with phase and momentum histograms, for a single bunch, without (blue) and with (red) the HHCs present in the storage ring for an 80% filling factor as four consecutive trains, for the 1st (top) and last (bottom) bunches of each train.

Filling pattern	Optimal phase	Bunch lengthening symmetry through the train	Maximum bunch lengthening factor
100%	96°	Symmetric	~ 3.6
80% as a single train	96°–97°	Rising through the first 30 bunches	~ 3
80% as four consecutive trains	96°–97°	Almost Symmetric	~ 3.3

**Table 5.** Summary of the bunch lengthening calculations.

displacement accuracy to 0.1 mm for the plunger enables significantly better phase shift precision. Therefore, the mechanical design of the plunger should support a displacement accuracy better than 0.1 mm.

The ILSF's second and third operation phases have beam currents of 250 mA and 400 mA, respectively. For these phases, a maximum bunch length of four to five times its primary value is expected by utilizing HHCs.

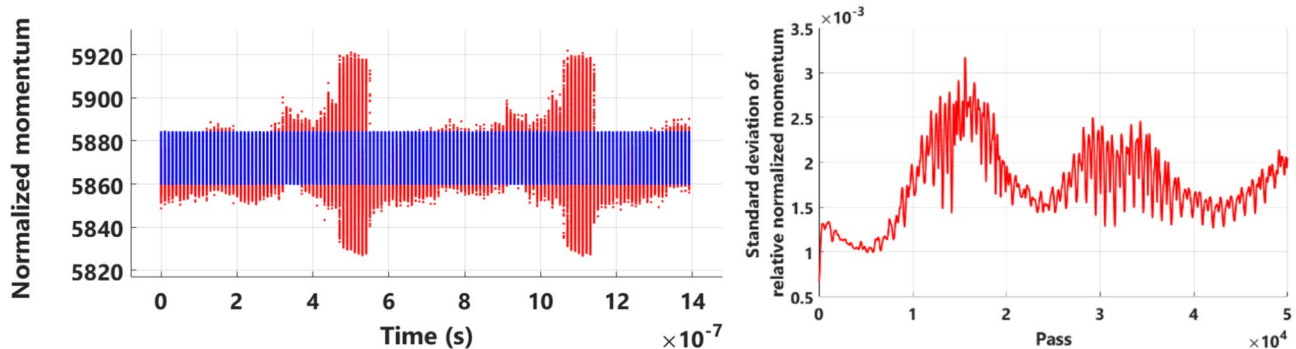


**Fig. 13.** (Color) Longitudinal particle distribution of the bunch train before (blue) and after (red) 50,000 turns in the storage ring, considering the main RF cavity HOMs, (left) and variations in the standard deviation of the train's relative normalized momentum during these 50,000 turns (right).

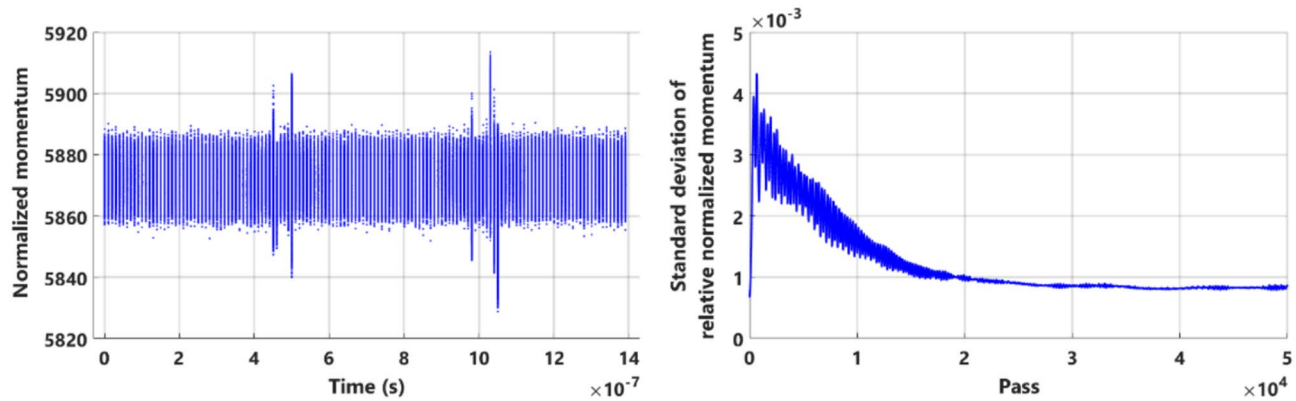


**Fig. 14.** Longitudinal particle distribution of the bunch train after 50,000 turns in the storage ring, considering both the main RF cavity HOMs and HHCs (left), and variations in the standard deviation of the train's relative normalized momentum during these 50,000 turns (right).

However, the HHCs will be further detuned to prevent the HHC's voltage from exceeding its optimal value, which would cause the bunches to be torn apart.

#### Effect on coupled bunch instabilities

Next, we study the effects of HHC on beam instabilities. This research focuses on the longitudinal instabilities caused by the longitudinal HOMs of the main RF cavity. These HOMs are detailed in our previous article on the ILSF's main RF cavity<sup>21</sup>. As a first step, we investigate the instabilities caused by these HOMs using particle tracking simulations with the ELEGANT code<sup>23</sup>. The simulation results indicate that the most destructive HOMs occur at frequencies of 1097.47 MHz, 1387 MHz, and 1432.55 MHz since the synchrotron oscillations in the storage ring do not naturally dampen the coupled bunch instabilities excited by these HOMs.

The simulations are conducted for two filling pattern scenarios in which 80% of the RF buckets are filled as a single bunch train and divided into four consecutive bunch trains spaced evenly apart. As of the ILSF's first phase of operation, the beam current is also 100 mA. In the initial stage of particle tracking simulations, the coupled bunch instabilities caused by the problematic HOMs mentioned earlier are examined for the single train filling pattern. The longitudinal particle distribution of the bunch train before and after 50,000 turns in the storage ring, considering the main RF cavity HOMs, is presented in Fig. 13 (left). Variations in the standard deviation of the train's relative normalized momentum ( $\sigma_\delta$ ) during these 50,000 turns are also displayed in Fig. 13 (right). As shown, the main RF cavity HOMs can induce significant coupled bunch instabilities, leading to complete beam loss within just a few seconds. The simulation results for the four-consecutive-trains pattern are even more severe than those for the single-train pattern.

After determining the effects of RF cavity HOMs on coupled bunch instabilities, the simulations are repeated with the presence of HHCs. Figure 14 illustrates the longitudinal particle distribution of the bunch train after 50,000 turns in the storage ring, considering both the main RF cavity HOMs and HHCs, and variations in the standard deviation of the train's relative normalized momentum ( $\sigma_\delta$ ) during these 50,000 turns. It is seen that the lengthening of bunches caused by the HHCs can nearly eliminate the coupled bunch instabilities triggered by the RF cavity HOMs, maintaining the beam current at a practically stable level and significantly extending its lifetime. The results are identical for the four consecutive trains pattern. However, the HHCs alone

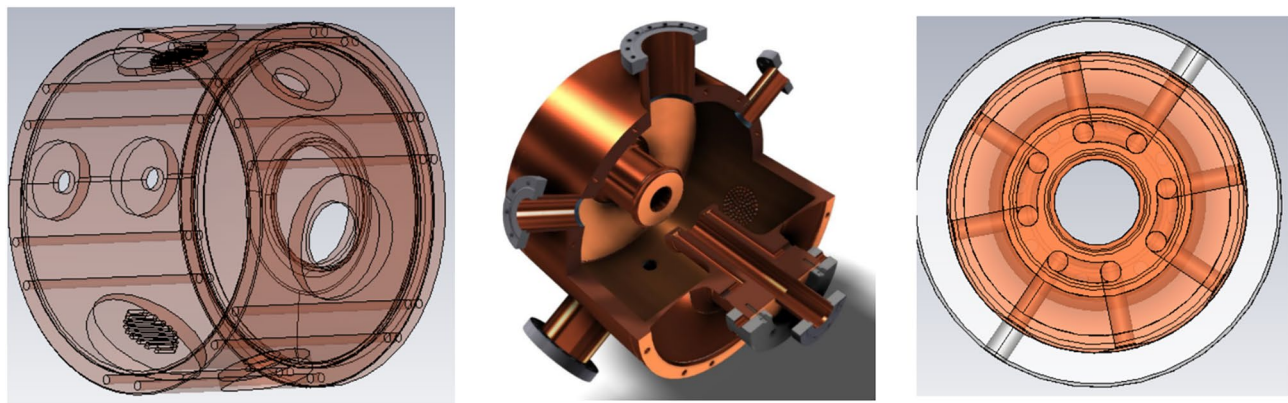


**Fig. 16.** Cooling pipes: Side wall (left), cross-section view of cavity (middle), and mushroom stem (right).

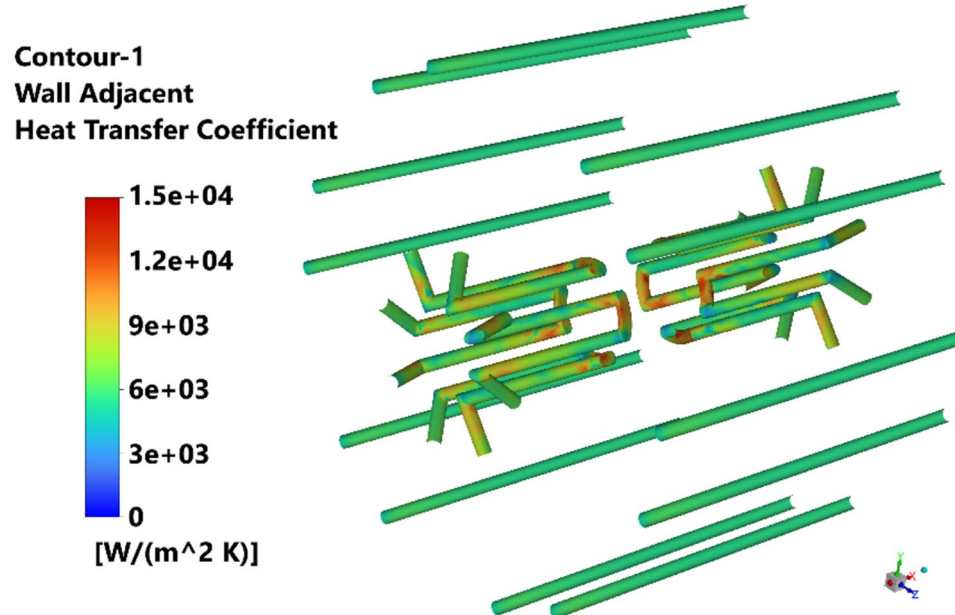


**Fig. 15.** Heat transfer coefficient inside the HHC's cooling water pipes, calculated by Ansys Mechanical<sup>24</sup>.

cannot maintain beam stability at higher beam currents. So, a fast bunch-by-bunch feedback system should be implemented to counteract coupled bunch instabilities in the storage ring.

### Thermo-mechanical simulations and design

The thermal and mechanical analysis of the HHC structure is conducted using Ansys Mechanical software (version 2019)<sup>24</sup>. The highest thermal dissipation on the HHC's body occurs at the end walls and the mushroom stem. Considering the potential power dissipation of the HHC's HOMs, the maximum power dissipation on the cavity body is overestimated to be 15 kW. The simulation model for the cooling pipes on the body, end walls, and mushroom stem of the HHC is shown in Fig. 16. Twelve water pipes are positioned along the lateral body, and eight paths are drilled into the mushroom stem. The diameter of the cooling pipes is 12 mm, and the minimum flow rate needed to achieve turbulent flow in the pipes is 1 m/s. Our simulations showed that the HHC's temperature can be maintained within a desired range by this flow rate. Therefore, since higher flow rates demand a more complex and costly cooling system, the water flow rate is set at 1 m/s. The heat transfer coefficient between the copper and water is calculated by the Ansys Mechanical software<sup>24</sup>, as shown in Fig. 15. The average heat transfer coefficient is approximately 6300 W/m<sup>2</sup>K. Additionally, the inlet water temperature is 20 °C, and the ambient temperature is assumed to be 23 °C (Fig. 16).

By declaring the boundary conditions for thermal analysis without accounting for the inverse pressure caused by the vacuum inside the cavity, the maximum Von-Mises stress is approximately 55.5 MPa, and the maximum total displacement of the cavity is about 0.052 mm at the end of the mushroom head. The maximum temperature on the body will reach 40.4 °C at the center of the end walls (see Fig. 17). After applying the vacuum

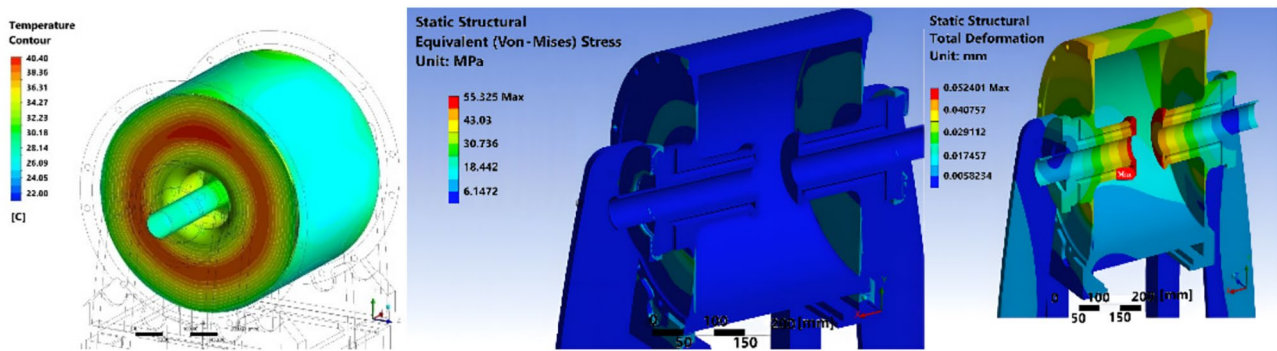


**Fig. 17.** (Color) Thermal simulation results: temperature distribution (left), Von-Mises stress (middle), and total deformation (right).

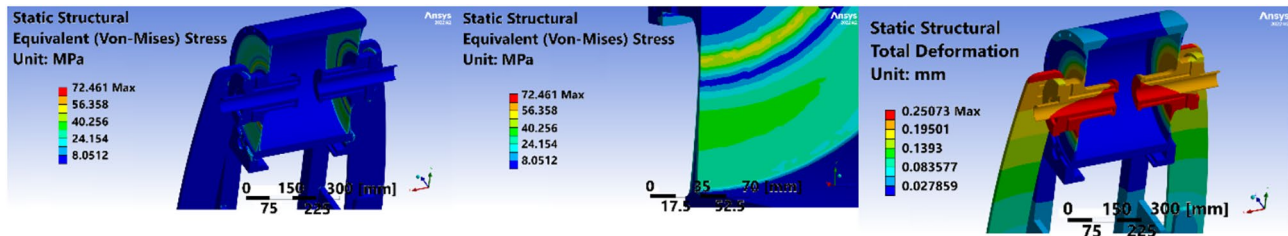


**Fig. 18.** (Color) Thermomechanical analysis considering both the power dissipation and vacuum: Von-Mises stress distribution (left), a view of stress distribution on the end wall's surface (middle), and the total deformation distribution (right).

conditions inside the cavity, the results presented in Fig. 18 indicate that the stress levels in the end walls of the cavity increase to 72.5 MPa, and the maximum deformation of the cavity is 0.25 mm. This deformation causes a frequency shift of approximately 280 kHz for the HHC. Thus, the reverse pressure on the cavity surfaces, resulting from volume evacuation, will significantly affect its resonant frequency. According to ASTM F68 standards for half-hard temper copper of grade C10100, the allowable yield stress in the material ranges between 150 and 200 MPa<sup>25</sup>. The simulation results demonstrate that a cooling system with the selected parameters will prevent severe stress in the thinning zone of the cavity's end walls.

A critical point during the cavity operation is the alignment of the two mushroom stems. Non-axial symmetry and transverse displacements may occur due to changes in temperature and the weight of the central components. By applying appropriate boundary conditions and constraining the two lower ends of the cavity, the displacement contours are plotted on the inner and outer surfaces of the cavity's end walls (see Fig. 18). The results indicate that the most considerable amount of displacement occurs in the longitudinal direction of the central axis, while the downward deviation of the middle sections is negligible. To enhance the performance of the frequency tuning mechanism through the displacement of the two end walls, the thickness of the end walls is reduced to 2.5 mm at the thinnest section. The simulation geometry and thin wall image are illustrated in Fig. 19.

In addition to previous evaluations, various studies have examined the impact of the thickness of the thinner zones of the end wall on stress and total deformation. Figure 21 presents the displacement and stress on the end walls for various thicknesses at a 20 °C inlet water temperature. The results indicate that reducing the thickness of this region increases both the longitudinal displacement and the Von-Mises stress. Due to technical requirements for vacuum and machining, the final thickness of this area is selected to be 3 mm.

The calculations indicate that each wall can be returned to its original position after the specified displacements are applied using a force of 7 kN. As a result, the engine and gearbox design for the frequency tuning mechanism has been designed to produce the required force when connecting the mechanical arms to the end walls (see Figs. 19 and 20). The gearbox ratio is 35:1, and the required torque at the gearbox output to generate a total force of 14 kN at the mechanical arms is approximately 100 Nm. Therefore, the motor must deliver a maximum torque of about 3 Nm. The Autonics A63K-M5913W stepper motor is selected for the tuning setup<sup>26</sup>. This motor can deliver a maximum torque of 6.3 Nm and has a full/half step angle of 0.72°/0.36° (Fig. 21).

### Vacuum analysis and design

This section examines the vacuum system for the HHC. Various studies and simulations have been conducted regarding the available pumping capabilities. This section compares the cross-section effect of the vacuum grooves on conductance and pressure profiles before and after thermal baking. It also compares system performance with two 100 l/s ion pumps versus one 240 l/s ion pump.

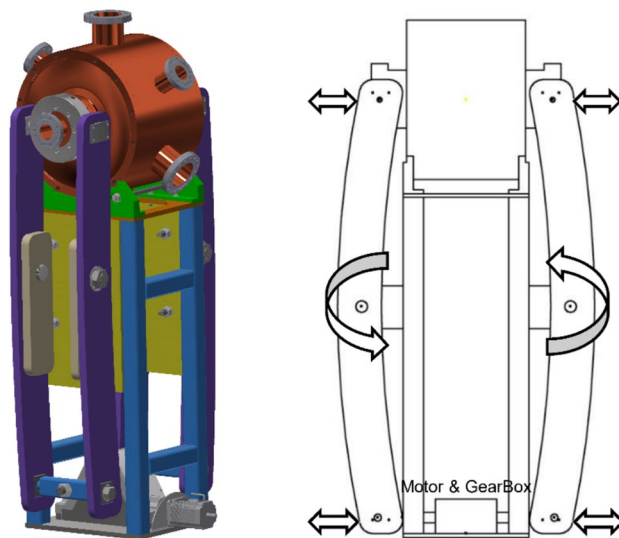


**Fig. 19.** Mechanical model and operation mechanism of the tuning setup.

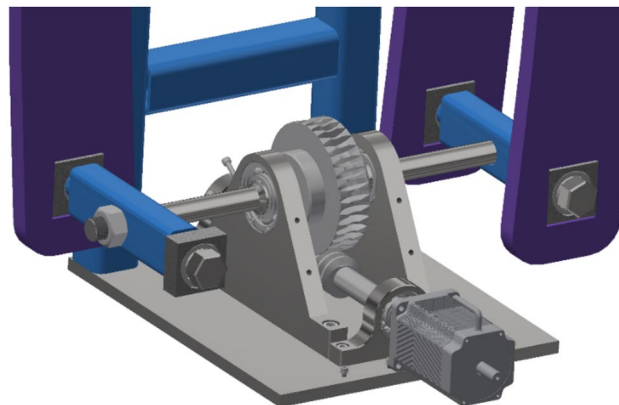


**Fig. 20.** Gearbox and motor design for the tuning setup.

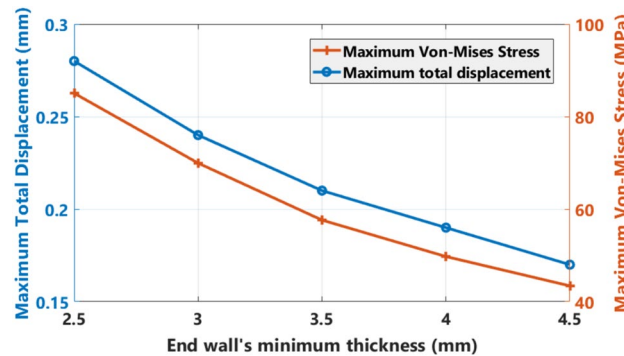


**Fig. 21.** (Color) The impact of the end wall's minimum thickness on displacement and stress.

The probability of either elastic or inelastic collisions between the electron beam and residual gas molecules in the vacuum chamber partially determines the lifetime of the electron beam in synchrotron light sources. Therefore, achieving a vacuum pressure of  $10^{-9}$  to  $10^{-10}$  mbar is essential for any component in the synchrotron storage rings. Figure 22 illustrates the geometry of the two vacuum ports, which have a speed of 100 l/s, located

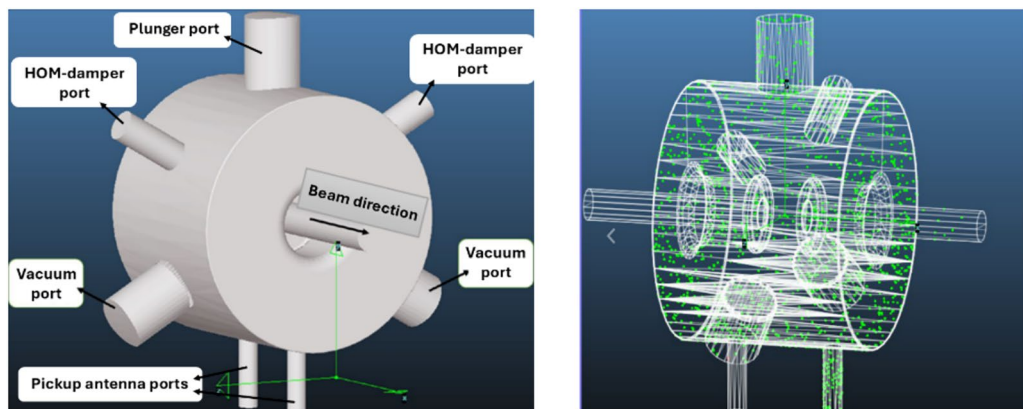


**Fig. 22.** Cavity geometry in the MolFlow vacuum simulation code with two CF100 flanges for 100 l/s ion pumps.

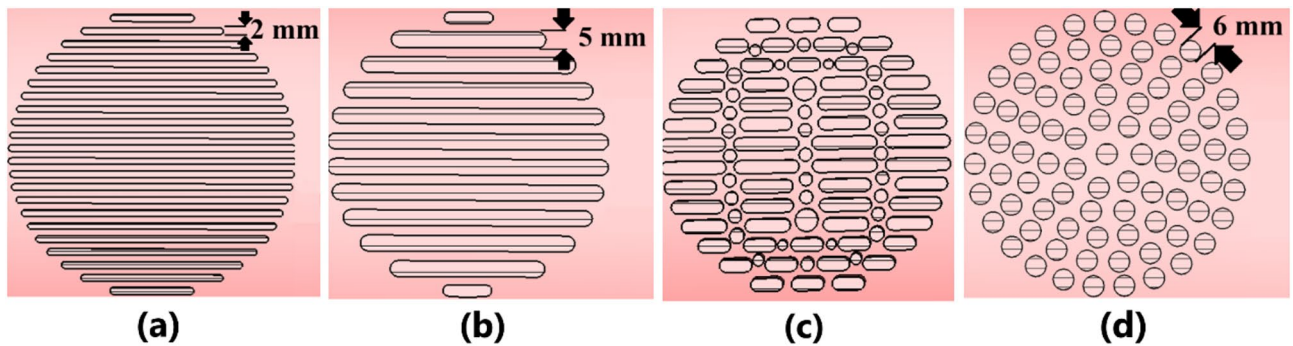


**Fig. 23.** Different studied cross-sections of vacuum grooves: small oval (a), large oval (b), oval and circle (c), circle (d).

Cross section	Vacuum conductance (l/s)
Small oval	105.3
Large oval	110.3
Oval and circle	101
Circle	98.4

**Table 6.** Vacuum conductance for different studied cross-sections.

on the HHC body. Various geometries for vacuum grooves on the surface interface of the vacuum ports have been explored to achieve improved conductance and pressure profiles (see Fig. 23).

MolFlow software (version 2.8.6)<sup>26</sup> is used to calculate the vacuum conductance of the grooves. The RF cavities of the storage ring operate under ultra-high vacuum pressure, and molecules behave according to the molecular flow regime. As a result, the conductance relies solely on the geometry and the molar mass of the residual gas. The calculated conductance values using MolFlow<sup>27</sup> for various cross-sections of vacuum grooves are displayed in Table 6.

Two 100 l/s diode ion pumps will serve as the cavity vacuum system. Based on the standard performance charts, the speed of these pumps at a pressure of 1 ntorr is 67 l/s. Depending on the port's conductivity, the effective pumping speed is calculated to be approximately 40 l/s, according to Eq. (6). In this equation,  $S_{eff}$ ,  $S_0$ , and  $C$  represent the effective pumping speed, nominal pumping speed, and vacuum conductance, respectively.

A diaphragm and turbomolecular pump setup is used as the backing pump station. Being oil-free, the diaphragm pumps lower contamination risks. Ion pumps generally start working effectively within a pressure range of  $10^{-5}$  to  $10^{-6}$  mbar. The backing pump station is used to reach a pressure of  $10^{-6}$  mbar. Once this pressure is achieved, ion pumps can begin operating, thereby facilitating to reach of the required vacuum conditions.

$$\frac{1}{S_{eff}} = \frac{1}{S_0} + \frac{1}{C} \quad (6)$$

Type of cross-section	Maximum pressure (mbar)	Average pressure (mbar)
Small oval	$1.13 \times 10^{-9}$	$1.11 \times 10^{-9}$
Large oval	$9.88 \times 10^{-10}$	$9.64 \times 10^{-10}$
Oval and circle	$1.06 \times 10^{-9}$	$1.03 \times 10^{-9}$
Circle	$1.17 \times 10^{-9}$	$1.05 \times 10^{-9}$

**Table 7.** Maximum and average pressures for the different studied cross-sections.

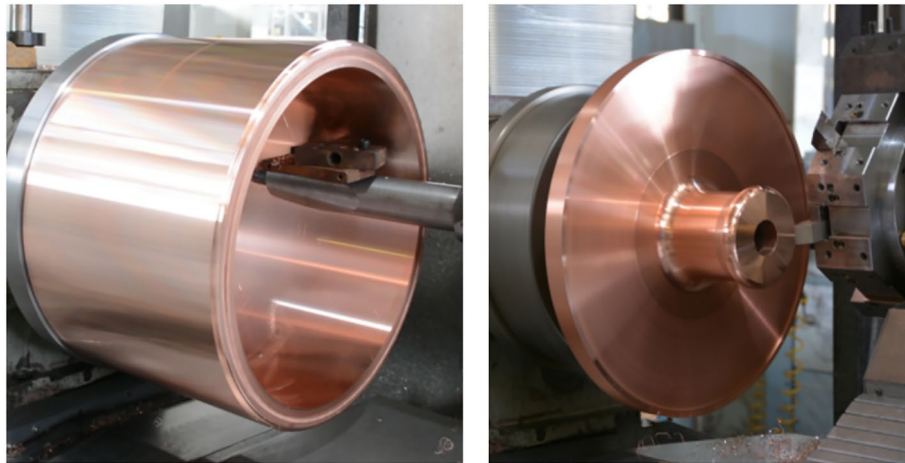


**Fig. 24.** The cylindrical body (left) and end walls of the HHC, fabricated separately.

After calculating the conductance and considering the pumping speed of the ion pumps along with the thermal desorption value, the pressure profile in different geometries can be obtained using MolFlow<sup>27</sup>.

All substances exposed to ultra-high vacuum desorb their surface gases into the vacuum system. This phenomenon occurs because the surfaces of the vacuum components are coated with several layers of different gas molecules that are temporarily adsorbed through physical and chemical reactions. The rate of thermal desorption can be defined as the base pressure of the vacuum system, regardless of synchrotron radiation. Desorption equals the amount of exhausted gas from a unit of solid surface per unit of time at a given pressure. The specific rate of desorption depends on the materials of the compartment, the fabrication quality, and the effectiveness of surface cleaning. For clean and post-annealed copper chambers at 150 °C and steel chambers at 250 °C, the specific desorption rate is assumed to be  $q = 1 \times 10^{-11} \text{ torrls}^{-1} \text{ cm}^{-2}$ . The simulation results for average and peak worth pressure for baked cavities are reported in Table 7.

According to the calculation results, the best performance is observed with the large oval cross-section of the vacuum grooves. Next, we estimate the performance of the cavity when heat baking is not performed and the cavity is in its initial stage after fabrication. When baking is not applied to steel or copper chambers, the desorption coefficient, which depends on the level of chemical and physical cleaning, ranges between  $q = 1 \times 10^{-9} \text{ torrls}^{-1} \text{ cm}^{-2}$  to  $q = 1 \times 10^{-10} \text{ torrls}^{-1} \text{ cm}^{-2}$ . For this estimation, we assumed the desorption coefficient to be equal to  $q = 5 \times 10^{-10} \text{ torrls}^{-1} \text{ cm}^{-2}$ . Under these conditions, the maximum and average pressures will be  $5 \times 10^{-8}$  and  $4.6 \times 10^{-8}$  mbar, respectively.

### Fabrication and measurements

For the development of the first HHC prototype, the cylindrical body and end walls were first fabricated separately. The body was formed by annealing and roll-forming a copper plate, followed by CNC machining to achieve the desired mechanical tolerances. The end walls and mushrooms were CNC machined from copper plates and rods and then brazed together. After brazing, the end walls were re-machined using CNC technology to meet the permitted mechanical tolerances. The cylindrical body and end walls of the HHC are shown in Fig. 24. Before the final brazing of all the parts, the end walls, cylindrical body, and various ports were secured together with steel screws for low-power RF measurements (see Fig. 25-left). Additionally, a loop antenna was fabricated and inserted into one of the HHC ports for low-power measurements.

After the initial low-power RF measurements, all HHC components were brazed together. Figure 25 shows the HHC before and after the final brazing and illustrates the bead pull measurement setup. Table 8 presents the simulated and measured resonance frequency, intrinsic quality factor, and shunt impedance of the HHC before and after the final brazing. Figure 26 displays the normalized E-field along the HHC's beam axis before and after the final brazing, evaluated through bead pull measurements.

After the low-power RF measurements, all cavity beam pipes and ports (except for the one used for the vacuum pump) were sealed with copper gaskets and steel flanges. A helium leak detector was employed to



**Fig. 25.** The HHC parts screwed together for low-power RF measurements (left) and after the final brazing (right). The bead pull measurement setup is also illustrated in the figures.

Resonance frequency (MHz)			Q (intrinsic)			RS (via R/Q, MΩ)		
Simulation (CST Studio Suite)	Measurement before the final brazing	Measurement after the final brazing	Simulation (CST Studio Suite)	Measurement before the final brazing	Measurement after the final brazing	Simulation (CST Studio Suite)	Measurement before the final brazing	Measurement after the final brazing
300.15	299.93	302.94	23,000	19,260	19,920	6.92	5.8	6

**Table 8.** Simulated and measured RF parameters of the HHC before (up) and after (down) the final brazing.

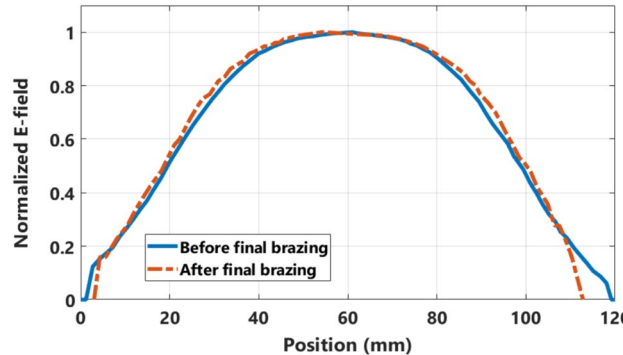


**Fig. 26.** (Color) Measured normalized E-field along the HHC's beam axis before (solid line-blue) and after (dashed line-red) the final brazing.

conduct the vacuum leak test on the HHC. Unfortunately, a small leak was discovered in one of the beam pipes, preventing the HHC from achieving vacuum pressures below the  $10^{-7}$  mbar range. The leak likely occurred during the brazing process, and it was determined that more precautions should be taken in the brazing of the second prototype to avoid such problems.

### Longitudinal HOMs of the HHC

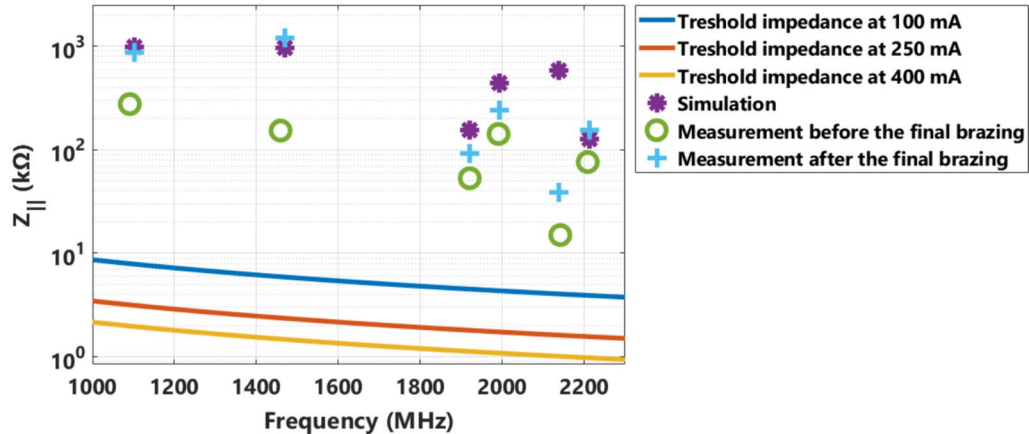
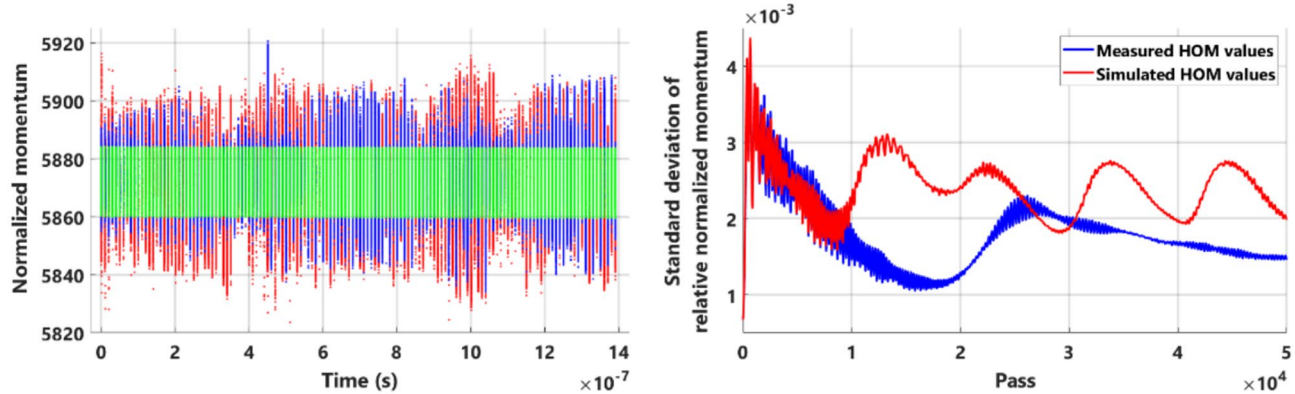
The simulated and measured values for shunt impedance and the quality factor of longitudinal HOMs are listed in Table 9. The shunt impedances, compared to the threshold impedances for synchrotron radiation damping at various beam currents, are depicted in Fig. 27. The threshold impedances are calculated using the following equation<sup>20</sup>:

$$Z_{||} = \frac{2 * Q_s * E_0 / e}{N_c f I_b \alpha \tau_s} \quad (7)$$

In this equation  $Q_s$ ,  $E_0$ ,  $e$ ,  $N_c$ ,  $f$ ,  $I_b$ ,  $\alpha$ , and  $\tau_s$  are synchrotron tune, beam energy, electron charge, number of cavities, frequency, beam current, momentum compaction factor, and synchrotron damping time, respectively.

Since all HOMs' shunt impedances are above the threshold impedances for synchrotron radiation damping, beam dynamics calculations are necessary to ensure beam stability in the storage ring. The coupled bunch instabilities caused by these HOMs are examined using particle tracking simulations with the ELEGANT code<sup>23</sup>.

Frequency (MHz)			Quality factor			Shunt impedance (kΩ)		
Simulation	Measurement before the final brazing	Measurement after the final brazing	Simulation	Measurement before the final brazing	Measurement after the final brazing	Simulation	Measurement before the final brazing	Measurement after the final brazing
1101.21	1090.94	1091.51	36,269	10,255	32,472	978	276	875
1469.16	1459.05	1457.29	37,806	6014	47,296	962	153	1203
1919.67	1920.67	1910.54	44,667	15,365	26,557	154	53	91
1992.53	1991.06	1981.88	47,772	15,597	26,659	436	142	243
2138.49	2141.82	2144.48	44,324	1125	2890	584	15	39
2212.74	2208.76	2206.06	39,530	23,770	49,085	126	76	156

**Table 9.** Simulated and measured values of longitudinal HOM characteristics.**Fig. 27.** (Color) The shunt impedances compared to the threshold impedances for synchrotron radiation damping at beam currents of 100, 250, and 400 mA.**Fig. 28.** (Color) Longitudinal particle distribution of the bunch train before (green) and after 50,000 turns in the storage ring, considering simulated (red) and measured (blue) HOM values of the HHCs (left), and variations in the standard deviation of the train's relative normalized momentum during these 50,000 turns (right), for an 80% filling factor as a single train.

As before, the simulations are run for two filling pattern scenarios: an 80% filling factor as a single bunch train and divided into four consecutive bunch trains spaced evenly apart. The beam current remains at 100 mA during the ILSF's first phase of operation.

The coupled bunch instabilities caused by the simulated and measured HOM values of the HHCs are analyzed. The longitudinal particle distribution of the bunch train before and after 50,000 turns in the storage ring, considering both the simulated and measured HOM values of the HHCs for each filling pattern scenario, is shown in Figs. 28 (left) and 29 (left). Changes in the standard deviation of the train's relative normalized momentum ( $\sigma_\delta$ ) over these 50,000 turns are also shown in Figs. 28 (right) and 29 (right). As demonstrated, the

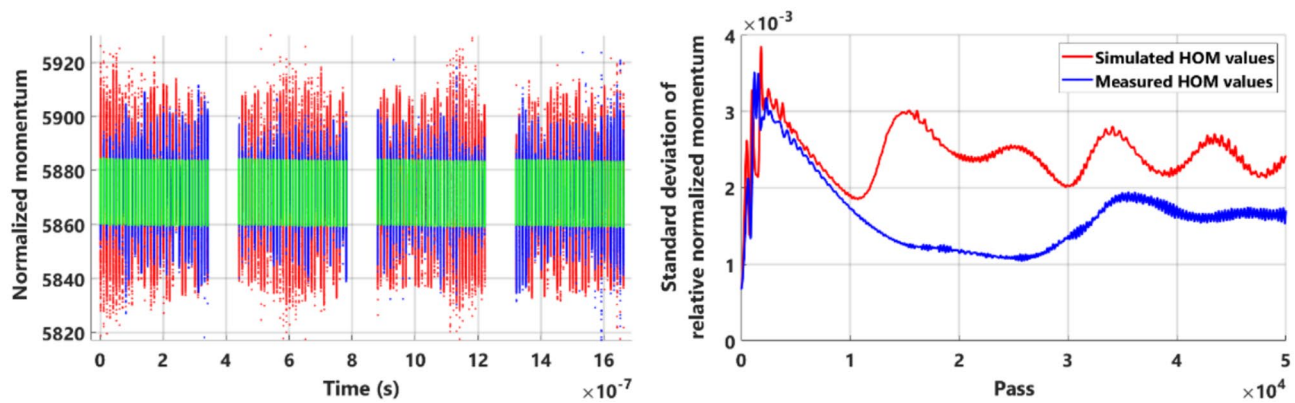


**Fig. 29.** (Color) Longitudinal particle distribution of the bunch train before (green) and after 50,000 turns in the storage ring, considering simulated (red) and measured (blue) HOM values of the HHCs (left), and variations in the standard deviation of the train's relative normalized momentum during these 50,000 turns (right), for an 80% filling factor as four consecutive trains.

simulated HOM values of the HHC lead to coupled bunch instabilities, but they stay within a limited range, making them manageable by the longitudinal feedback system. Fortunately, these HOMs are not as strong as initially expected, as the measured HOM values cause far fewer instabilities, allowing the longitudinal feedback system to suppress them without any difficulty.

### Conclusions and outlook

This paper presents the analytical calculations and simulations of beam dynamics, as well as the electromagnetic, thermomechanical, and vacuum aspects of the Higher Harmonic Cavities (HHCs) at the Iranian Light Source Facility (ILSF). HHCs are widely used in advanced synchrotron storage rings to increase the bunch length, thereby expanding the stored beam's lifetime and eliminating coupled bunch instabilities. The specifications for certain advanced synchrotron HHCs are summarized in Table 2.

The HHCs at ILSF are passive, capacitive-loaded structures designed to operate at 300 MHz and within a beam current range of 50–400 mA. They have a shunt impedance of approximately  $6\text{ M}\Omega$  and a quality factor of around 20,000. The key strength of this paper lies in its comprehensive and multi-disciplinary approach, which is seldom addressed in previous publications. Notably, we employed the ELEGANT code<sup>23</sup> for beam dynamics simulations, providing a more robust and detailed analysis compared to the predominantly analytical methods used in earlier studies.

The beam dynamics calculations show that during ILSF's first operation phase, with a beam current of 100 mA, three HHCs installed in the storage ring can increase the bunch length by at least three times and fully counteract the coupled bunch instabilities caused by the main RF cavity HOMs. These calculations examine three different filling pattern scenarios: all RF buckets in the storage ring are evenly filled with electron bunches, only 80% of the RF buckets are filled as a single bunch train, and 80% of the RF buckets are filled with four consecutive bunch trains spaced equally apart. The studies show that in the second scenario, the HHC's voltage takes approximately 300 ns to reach its final steady-state value, resulting in the first 30 bunches of each train experiencing suboptimal bunch lengthening. Nevertheless, this issue is resolved in the third scenario, where the gap between consecutive bunch trains is only 90 ns, preventing the HHC's voltage from damping thoroughly, which results in a semi-uniform longitudinal particle distribution throughout all bunches in the storage ring.

After finalizing the engineering drawings, the first prototype was developed for vacuum and low-power RF measurements. The HHC's HOMs are also measured, compared to the simulation results, and their effects on the coupled bunch instabilities in the storage ring are calculated and presented. Fortunately, these HOMs are not as strong as initially simulated, as the measured HOM values cause far fewer instabilities, allowing the longitudinal feedback system to suppress them without any difficulty. Regrettably, a leak in one of the beam pipes prevented the HHC from achieving vacuum pressures below the  $10^{-7}$  mbar range, indicating that more precautions are necessary during the brazing process. This challenge is under further investigation at ILSF for the development of the second prototype.

### Data availability

The data that support the findings of this study are available from the corresponding author, M. Ostovar (mohammad.ostovar@ipm.ir), upon reasonable request.

Received: 5 April 2025; Accepted: 5 September 2025

Published online: 08 October 2025

## References

1. Rahighi, J. *et al.* Progress status of the Iranian light source facility. In *Proceedings of 5th International Particle Accelerator Conference, Dresden, Germany, June 16–20*, 2861–2863. <https://doi.org/10.18429/JACoW-IPAC2014-MOPRO069> (2014).
2. Rahighi, J. *et al.* Recent progress on the development of Iranian Light Source Facility (ILSF) project. In *Proceedings of 7th International Particle Accelerator Conference, BEXCO, Busan, South Korea, May 8–13*, 1137–1139. <https://doi.org/10.18429/JACoW-IPAC2016-WEPOW017> (2016).
3. Sadeghipanah, A. *et al.* Low emittance pre-injection system for Iranian Light Source Facility. *Nucl. Inst. Methods Phys. Res. A* **806**, 340–347. <https://doi.org/10.1016/j.nima.2015.10.062> (2016).
4. Sadeghipanah, A. *et al.* Bunch compression in low emittance pre-injection system of Iranian Light Source Facility *Jinst.* **11**, P01002. <https://doi.org/10.1088/1748-0221/11/01/P01002> (2016).
5. Ghasem, H. *et al.* Beam dynamics of a new low emittance third generation synchrotron light source facility. *Phys. Rev. Spec. Top. Accel. Beams* **18**, 030710. <https://doi.org/10.1103/PhysRevSTAB.18.030710> (2015).
6. Ghasem, H., Ahmadi, E., & Saeidi, F. Lattice design history of the Iranian Light Source Facility storage ring. In *Proceedings of 5th International Particle Accelerator Conference, Dresden, Germany, June 16–20*, 249–251. <https://doi.org/10.18429/JACoW-IPAC2014-MOPRO072> (2014).
7. Phimsen, T. *et al.* Improving Touschek lifetime and synchrotron frequency spread by passive harmonic cavity in the storage ring of SSRF. *Nucl. Sci. Tech.* **28**, 108. <https://doi.org/10.1007/s41365-017-0259-y> (2017).
8. Cullinan, F. J., Andersson, A., & Tavares, P. F. Review of harmonic cavities in fourth-generation storage rings. In *67th ICFA Adv. Beam Dyn. Workshop Future Light Sources, FLS2023, Luzern, Switzerland*. <https://doi.org/10.18429/JACoW-FLS2023-MO2L3>.
9. Cullinan, F. J., Andersson, A., & Tavares, P. F. Harmonic-cavity stabilization of longitudinal coupled-bunch instabilities with a nonuniform fill. *Phys. Rev. Accel. Beams* **23**, 074402. <https://doi.org/10.1103/PhysRevAccelBeams.23.074402> (2020).
10. Tavares, P. F., Andersson, Å., Hansson, A., & Breunlin, J. Equilibrium bunch density distribution with passive harmonic cavities in a storage ring. *Phys. Rev. Accel. Beams* **17**, 064401. <https://doi.org/10.1103/PhysRevSTAB.17.064401> (2014).
11. Pérez, F. *et al.* ALBA II Accelerator upgrade project, 13th international particle accelerator conference, Bangkok, Thailand <https://doi.org/10.18429/JACoW-IPAC2022-TUPOMS027> (2022).
12. Karantzoulis, E., Fabris, A., Krecic, S. The ELETTRA 2.0 project. In *13th International Particle Accelerator Conference, Bangkok, Thailand*. <https://doi.org/10.18429/JACoW-IPAC2022-TUPOMS023> (2022).
13. Dastan, S., Karantzoulis, E., Manukyan, K., Krecic, S. Broad band impedance effects on Elettra 2.0-Inspire HEP. In *14th International Particle Accelerator Conference, Venice, Italy*. <https://doi.org/10.18429/JACoW-IPAC2023-MOPM051> (2023).
14. Zhang, P. *et al.* Radio-frequency system of the high energy photon source. *Radiat. Detect. Technol. Methods*. <https://doi.org/10.1007/s41605-022-00366-w> (2022).
15. Wu, W.-B. *et al.* Development of a control system for the fourth-harmonic cavity of the HLS storage ring. *Nucl. Sci. Tech.* **29**. <https://doi.org/10.1007/s41365-018-0497-7> (2018).
16. D'Elia, A., Serrière, V., Jacob, J., & Zhu, X. Design of 4th harmonic RF cavities for ESRF-EBS. In *12th International Particle Accelerator Conference, Campinas, SP, Brazil*. <https://doi.org/10.18429/JACoW-IPAC2021-MOPA332> (2021).
17. Ahmadiannamin, S. *et al.* Behaviour analysis of a capacitive loaded RF cavity for the Iranian Light Source Facility (ILSF). *JINST* **14**, T07003. <https://doi.org/10.1088/1748-0221/14/07/T07003> (2019).
18. Poisson Superfish version 7.1. <https://poisson-superfish.software.informer.com/7.1/>
19. CST Studio Suite version 2024. <https://www.3ds.com/products/simulia/cst-studio-suite>
20. Kilpatrick, W. D. Criterion for vacuum sparking designed to include both rf and dc. *Rev. Sci. Instrum.* **28**(10), 824–826. <https://doi.org/10.1063/1.1715731> (1957)
21. Ahmadiannamin, S. *et al.* Design of 100 MHz RF cavity for the storage ring of the Iranian Light Source Facility (ILSF). *Nucl. Instrum. Method. A*. <https://doi.org/10.1016/j.nima.2020.164529> (2020).
22. Byrd, J. M. & Georgsson, M. Lifetime increase using passive harmonic cavities in synchrotron light sources. *Phys. Rev. Spec. Top. Accel. Beams* **4**, 030701. <https://doi.org/10.1103/PhysRevSTAB.4.030701> (2001).
23. ELEGANT accelerator code version April 9, 2024. <https://www.aps.anl.gov/Accelerator-Operations-Physics/Software>
24. Ansys Mechanical version 2019. <https://www.ansys.com/products/structures/ansys-mechanical>
25. LUVATA datasheet for Oxygen-free electronic grade copper Cu-OFE-LUVATA alloy OFE-OK. [https://www.luvata.com/docs/default-source/products/alloy-data-sheets/oxygen-free-electronic-grade-copper\\_ofe-ok\\_eng.pdf](https://www.luvata.com/docs/default-source/products/alloy-data-sheets/oxygen-free-electronic-grade-copper_ofe-ok_eng.pdf)
26. Autonics page for A63K-M5913W stepper motor. <https://www.autonics.com/glb/model/A63K-M5913W>
27. MolFlow version 2.8.6. <https://doi.org/10.18429/JACoW-IPAC2019-TUPMP037>

## Acknowledgements

The authors would like to thank Prof. R. Bartolini for his insightful comments and constructive discussions on this project. They also express gratitude to Kh. Sarhadi, head of the ILSF RF group, and J. Dehghani, head of the ILSF Mechanics group, for their support. We appreciate the ILSF Mechanics group for their assistance.

## Author contributions

A.S.: Formal analysis, investigation, validation, visualization writing-review and editing. S.A.: Conceptualization, formal analysis, investigation, software, writing-original draft. M.O.: Formal analysis, investigation, validation, visualization. A.B.: Formal analysis, software. V.M.: Formal analysis, investigation, software. S.T.M.: Formal analysis, investigation, software. J.R.: Formal analysis, investigation, validation. B.A.A.: Methodology validation.

## Declarations

### Competing interests

The authors declare no competing interests.

### Additional information

**Correspondence** and requests for materials should be addressed to M.O.

**Reprints and permissions information** is available at [www.nature.com/reprints](http://www.nature.com/reprints).

**Publisher's note** Springer Nature remains neutral with regard to jurisdictional claims in published maps and institutional affiliations.

**Open Access** This article is licensed under a Creative Commons Attribution-NonCommercial-NoDerivatives 4.0 International License, which permits any non-commercial use, sharing, distribution and reproduction in any medium or format, as long as you give appropriate credit to the original author(s) and the source, provide a link to the Creative Commons licence, and indicate if you modified the licensed material. You do not have permission under this licence to share adapted material derived from this article or parts of it. The images or other third party material in this article are included in the article's Creative Commons licence, unless indicated otherwise in a credit line to the material. If material is not included in the article's Creative Commons licence and your intended use is not permitted by statutory regulation or exceeds the permitted use, you will need to obtain permission directly from the copyright holder. To view a copy of this licence, visit <http://creativecommons.org/licenses/by-nc-nd/4.0/>.

© The Author(s) 2025, corrected publication 2025